Weak Lensing in the Blue: A Counter-intuitive Strategy for Stratospheric Observations

Mohamed M. Shaaban[1,2], Ajay S. Gill[1,3], Jacqueline McCleary[4], Richard J. Massey[5,6,7], Steven J. Benton[8], Anthony M. Brown[6,7], Christopher J. Damaren[9], Tim Eifler[10], Aurelien A. Fraisse[8], Spencer Everett[11], Mathew N. Galloway[12], Michael Henderson[9], Bradley Holder[1,9], Eric M. Huff[11], Mathilde Jauzac[5,6], William C. Jones[8], David Lagattuta[6], Jason S.-Y. Leung[1,3], Lun Li[8], Thuy Vy T. Luu[8], Johanna M. Nagy[13,14], C. Barth Netterfield[1,2,3], Susan F. Redmond[8], Jason D. Rhodes[11], Andrew Robertson[11], Jürgen Schmoll[7], Ellen Sirks[5], and Suresh Sivanandam[1,3]

[1] Dunlap Institute for Astronomy and Astrophysics, University of Toronto, 50 St. George Street, Toronto, ON, M5S 3H4, Canada; m.shaaban@mail.utoronto.ca
[2] Department of Physics, University of Toronto, 60 St. George Street, Toronto, ON, M5R 2M8, Canada
[3] David A. Dunlap Dept. of Astronomy and Astrophysics, University of Toronto, 50 St. George Street, Toronto, ON, M5S 3H4, Canada
[4] Department of Physics, Northeastern University, 360 Huntington Avenue, Boston, MA, USA
[5] Institute for Computational Cosmology, Durham University, South Road, Durham DH1 3LE, UK
[6] Centre for Extragalactic Astronomy, Department of Physics, Durham University, Durham DH1 3LE, UK
[7] Centre for Advanced Instrumentation (CfAI), Durham University, South Road, Durham DH1 3LE, UK
[8] Department of Physics, Princeton University, Jadwin Hall, Princeton, NJ, 08544, USA
[9] University of Toronto Institute for Aerospace Studies (UTIAS), 4925 Dufferin Street, Toronto, ON, M3H 5T6, Canada
[10] Department of Astronomy/Steward Observatory, University of Arizona, 933 North Cherry Avenue, Tucson, AZ, 85721, USA
[11] Jet Propulsion Laboratory (JPL), California Institute of Technology, 4800 Oak Grove Drive, Pasadena, CA, 91109, USA
[12] Institute of Theoretical Astrophysics, University of Oslo, Blindern, Oslo NO-0315, Norway
[13] Department of Physics, Washington University in St. Louis, 1 Brookings Drive, St. Louis, MO, 63130, USA
[14] McDonnell Center for the Space Sciences, Washington University in St. Louis, 1 Brookings Drive, St. Louis, MO, 63130, USA

Abstract

The statistical power of weak lensing measurements is principally driven by the number of high-redshift galaxies whose shapes are resolved. Conventional wisdom and physical intuition suggest this is optimized by deep imaging at long (red or near-IR) wavelengths, to avoid losing redshifted Balmer-break and Lyman-break galaxies. We use the synthetic Emission Line ("EL")-COSMOS catalog to simulate lensing observations using different filters, from various altitudes. Here were predict the number of exposures to achieve a target $z \gtrsim 0.3$ source density, using off-the-shelf and custom filters. Ground-based observations are easily better at red wavelengths, as (more narrowly) are space-based observations. However, we find that SUPERBIT, a diffraction-limited observatory operating in the stratosphere, should instead perform its lensing-quality observations at blue wavelengths.

1. Introduction

The standard model of cosmology predicts that most of the energy density of the universe is dominated by dark energy and dark matter, both of which possess exotic physical properties that have only been weakly constrained. As a result, constraining the nature of dark energy and dark matter are considered two of the greatest challenges in contemporary science. Weak gravitational lensing is a powerful tool for probing the physics of dark matter and dark energy (Weinberg et al. 2013). Weak lensing occurs when light radiated from distant galaxies changes path as it passes through a foreground gravitational field. This change of path results in an apparent distortion of the galaxy image. Measuring this change in shape allows us to reconstruct the gravitational field and thus the distribution of (all) mass (Mandelbaum 2018). Mapping the large-scale structure of dark matter can constrain cosmological parameters (Haiman et al. 2001; Holder et al. 2001); mapping its distribution around specific entities such as galaxy clusters can also constrain cosmological parameters or test dark matter physics (Massey et al. 2010; Harvey et al. 2015;

Robertson et al. 2019). In practice, the original shape of the distorted galaxy is unknown, so weak lensing signals can only be inferred via statistical methods applied to ensembles of galaxies. With the weak lensing signal of a galaxy cluster constrained inside a small patch of sky, the signal-to-noise of cluster mass maps is driven by the spatial *density* of galaxies whose shapes can be measured and averaged.

Conventional wisdom dictates that one can maximize the density of high-redshft galaxies by observing at the red end of the spectrum. The physical intuition behind this is the desire to avoid losing redshifted Balmer-break and Lyman-break galaxies. However, the intuition can be violated by specific observing conditions, environment, and instrumental configurations. One example of an instrument for which this convention is violated is the Super-pressure Balloon-borne Imaging Telescope (SUPERBIT). SUPERBIT is a balloon-borne, diffraction-limited, wide-field, near-ultraviolet to near-infrared observatory designed to exploit the stratosphere's space-like conditions to perform deep lensing observations of galaxy clusters (Romualdez et al. 2019; Gill et al. 2020). The telescope has a $15' \times 23'$ field of view that is designed to capture a 4 Mpc diameter galaxy cluster at $z \geqslant 0.2$ in a single exposure. SUPERBIT has four broadband filters and two ultrabroadband filters covering a wavelength range from 300 to 900 nm. SUPERBIT plans to use either its broad blue band B or

Table 1
Summary of SUPERBIT's Relevant Specifications

Aperture	500 mm ($f/\# = 11$)
Obscuring Fraction	0.38
Collecting Area (A)	0.121 m^2
Focal Plane Jitter (1σ)	0.05″
Bandwidth	300–900 nm (See Figure 1)
Plate Scale	0.141″ pixel^{-1}
Dark Current at -20 C{°} (N_d)	0.002 e^- s^{-1} pixel^{-1}
Read Noise (N_r)	1.5 e^-

ultrabroad luminous band L for its deep lensing observations. The purpose of this paper is to provide justification for this seemingly unconventional choice by simulating artificial SUPERBIT observations of the COSMOS survey (Scoville et al. 2007) and comparing the relative performance of the bands.

2. Method

Any figure of merit to compare the performance of different filters is likely to track some aspect of image depth as a function of exposure time. For a weak lensing measurement, obtained statistically from ensembles of galaxies, a natural choice is the density of high-redshift galaxies that are both bright enough to be detected and large enough to be resolved. We shall equivalently adopt the observing time required to reach a target threshold in the density of such galaxies.

To compute this figure of merit, we simulate observations in a range of instrumental configurations and observing environments. The general procedure is as follows. First we fix instrument-specific parameters for the telescope optics and science detector (Section 2.1). Then we specify the observing environment and determine the flux from sky background that reaches the detector in all of the instrument's bands (Section 2.2). Finally we model the flux reaching the detector from distant galaxies (Section 2.3), using galaxies' spectral energy distributions (SEDs) from (Saito et al. 2020)'s synthetic Emission Line COSMOS (EL-COSMOS) catalog and morphologies from Mandelbaum et al. (2012)'s COSMOS-Galsim catalog. We apply cuts similar to those in a real cluster lensing analysis, requiring:

1. galaxy redshift $z > 0.3$;
2. galaxy flux signal-to-noise ratio (S/N) $\geqslant 5$ inside a fixed 3×3 pixel aperture;
3. galaxy half-light radius r_e greater than the full width at half maximum (FWHM) of the instrument's point-spread function (PSF).

Our figure of merit is calculated from the density of galaxies remaining after these cuts, as a function of exposure time.

2.1. Instrument Specifications

In this analysis we consider one set of system optics, with two different configurations of detector throughput and optical transmission. Our optics model matches the SUPERBIT telescope (Romualdez et al. 2020): a diffraction-limited 500 mm diameter telescope with 38% of the collecting area obscured by a secondary mirror, and a focal plane Gaussian jitter with $\sigma = 0.05''$. The first configuration of detector throughput (SUPERBIT configuration) comprises the nominal SUPERBIT science detector: the Sony IMX455 CMOS camera, with dark current of $0.002\,e\,\text{s}^{-1}\,\text{pixel}^{-1}$, read noise of $1.5\,e\,\text{pixel}^{-1}$, and sensitivity in the 300–900 nm range measured and presented in Gill et al. (2022). The second configuration (flat configuration) is a fictional configuration with noise specifications identical to the SUPERBIT configuration, but with a total transmission multiplied by quantum efficiency of $0.5\,e^-\,\text{photon}^{-1}$, irrespective of wavelength. This is to enable us to quantify the extent to which our results are dependent on the integrated QE curve shape. Both detector configurations adopt a plate scale of 0.141″ per pixel. For both configurations we model the system's PSF as the convolution of a diffraction-limited airy disk and a Gaussian kernel representing the system jitter. A summary of the relevant instrument specifications is presented in Table 1.

The final instrument specification of relevance to this analysis is the choice of photometric bandpasses. We perform this analysis in six bands. Four are SUPERBIT's nominal photometric bands: U (330–430 nm), B(370–570 nm), G (520–700 nm), and R(640–800 nm). The remaining two are broadbands, one of which is a near-red band that was the originally proposed deep lensing observation band: S (530–830 nm) that has been scrapped as a result of this analysis. The other is the near-blue band currently considered the deep lensing observation band L(400–700 nm). This band was determined using a band optimization tool that will be publicly released in an upcoming publication. The fully integrated bandpass curves for the SUPERBIT configuration are presented in Figure 1. Note that at the time of this analysis, the SUPERBIT science filters were still in the manufacturing process so only the median in-band throughput was known. As a result, the filters are taken to be boxcar with amplitude equal to the median throughput as provided by the vendor ($\geqslant 0.9$) and an out-of-band transmission of 0.

2.2. Observing Environment

The next step in the analysis is to model the observing environment. Specifically, we need to model the sky background level and atmospheric transmission for both instrument configurations in three distinct environments: the ground, the stratosphere, and low-earth orbit. While SUPERBIT will only collect data in the stratosphere, we include the other more familiar environments to serve as a reference for the reader.

For the model of sky background in the stratosphere, we use the measured average values from Gill et al. (2020). Specifically, we take the flux values at the pivot wavelength λ_p of each band in which the sky background was measured, defined as

$$\lambda_p^2 = \frac{\int (e_\lambda \lambda)\ \mathrm{d}\lambda}{\int (e_\lambda/\lambda)\ \mathrm{d}\lambda}\ , \qquad (1)$$

where e_λ is the product of the total in-band transmission and quantum efficiency as a function of wavelength, in units of e^- photon^{-1}. We then linearly interpolate the flux as a function of wavelength between the data points to generate an approximate model of the background SED in the stratosphere. While this method has its limitations, it suffices for this analysis as the bands of interest are similar in bandwidth and pivot wavelength to the bands in which the measurements were performed. For the sky
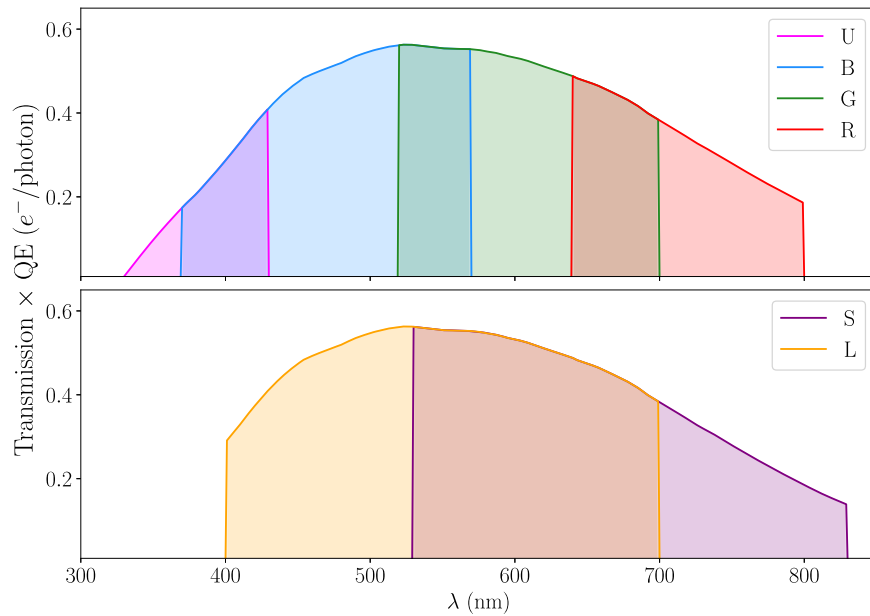
Figure 1. The overall SUPERBIT configuration bandpass that is constructed by taking the product of the throughput of all of SUPERBIT's optical elements, filter transmission, and science camera quantum efficiency. The top panel shows the bandpass for the photometric bands U (330–430 nm), B(370–570 nm), G(520–700 nm), and R(640–800 nm). The bottom panel shows the bandpass for the broadbands L(400–700 nm) and S(530–830 nm). The flat configuration bandpass would be simple a series of horizontal lines at 0.5.
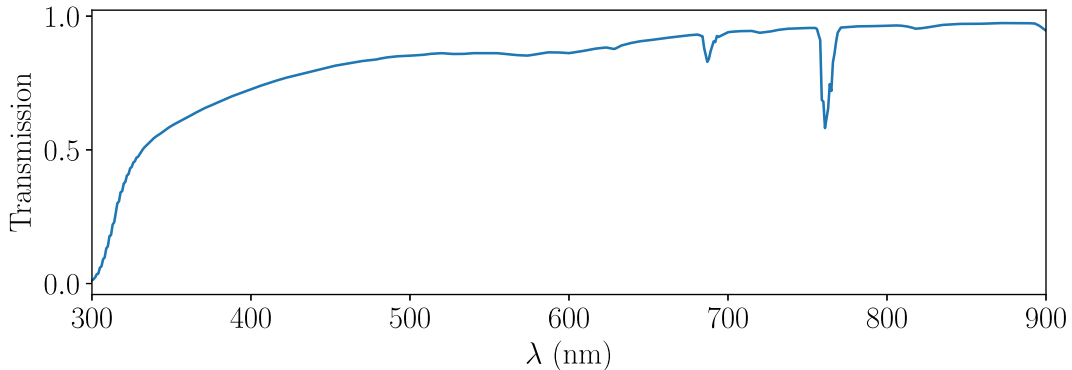
Figure 2. Atmospheric transmission at an altitude of 5 km above sea level in desert conditions at mid-latitude winter, as calculated by the MODTRAN webapp.

background model in low-earth orbit, we use the high sky background data publicly available in the WFC3 manual for the Hubble Space Telescope (HST; Dressel 2022). Finally, for the model of sky background from the ground, we use the publicly available optical background data for the Gemini Observatory.[15]

The atmospheric transmission in the bands of interest is taken to be order unity in the stratosphere and low-earth orbit. For the ground, we calculated the atmospheric transmission using the MODTRAN webapp[16] for an altitude of 5 km (Figure 2).

All three background models are presented in Figure 3. Note that the ground model is an empirical one and therefore the atmospheric transmission is already folded in. We only need to use our modeled transmission curve for simulating the observations of astronomical sources from the ground.

Once the environments are modeled, we calculate the total number of electrons per second, N_b, generated in each pixel of the detector by the sky background, as

$$N_b = AP^2 \int f_\lambda e_\lambda \ \mathrm{d}\lambda \,, \qquad (2)$$

where A is the total collecting area, P is the detector's pixel scale in arcseconds pixel^{-1}, f_λ is the source flux density as a function of wavelength, and e_λ is the product of the total in-band transmission and quantum efficiency as a function of wavelength in units of $e^-\,\mathrm{photon}^{-1}$. The calculated background electron flux for all configurations is presented in Figure 4. We note that the background flux per pixel for SUPERBIT in the stratosphere is significantly higher in S than L despite the comparable bandwidth. This long-wavelength sky background plays a major role in SUPERBIT's differential performance at red and blue wavelengths, as we will show in Section 3.

2.3. Source Galaxy Population

2.3.1. Which Galaxies are Bright Enough to be Detected?

The publicly available EL-COSMOS catalog (Saito et al. 2020) provides spectral energy distribution (SED) models of

---

[15] The Gemini Observatory background data used can be found at http://www.gemini.edu/observing/telescopes-and-sites/sites.

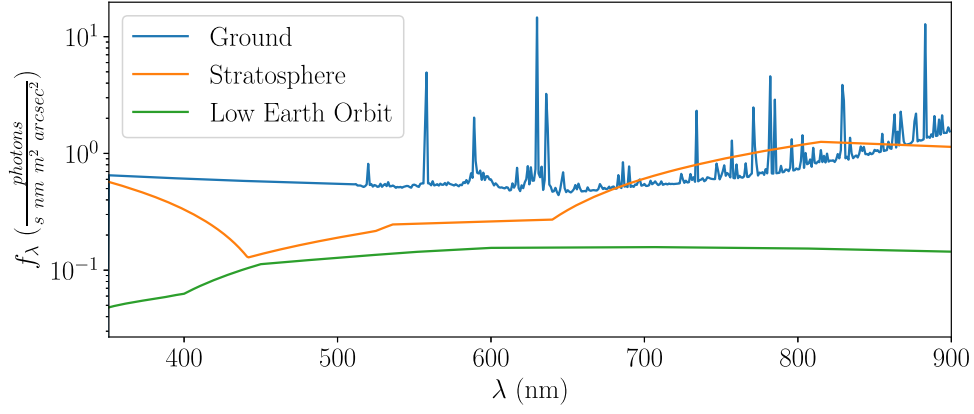[16] The MODTRAN webapp can be found here http://modtran.spectral.com/modtran_home.

Figure 3. The background flux density in units of $\frac{\text{photons}}{s\ nm\ m^2\ \text{arcsec}^2}$ at the aperture for the three environments considered.
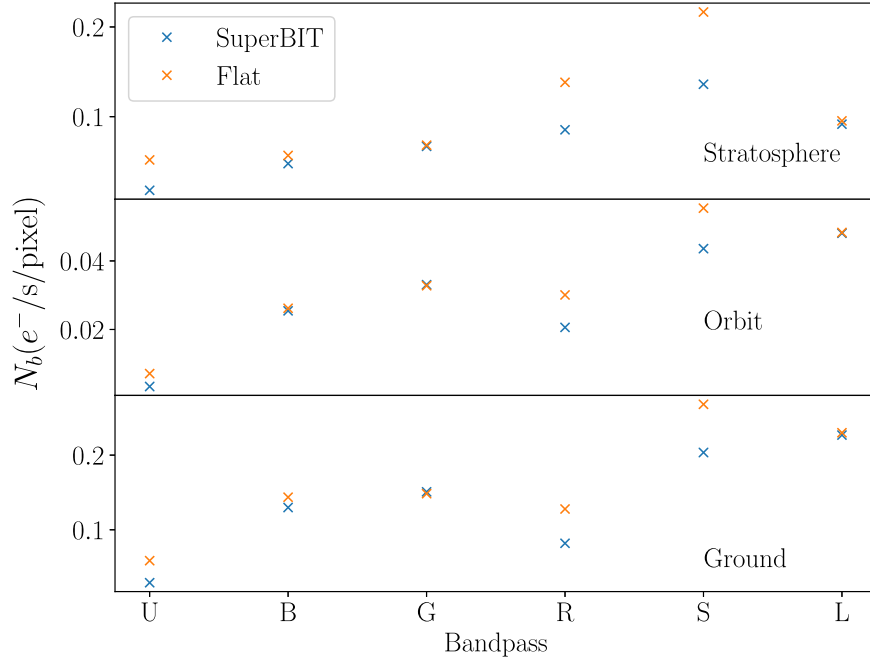

Figure 4. The modeled number of electrons per second per pixel, generated on a detector by the sky background, for the SUPERBIT (blue) and flat (orange) instrument configurations, in all three observing environments.

more than 500,000 galaxies from the COSMOS2015 catalog (Laigle et al. 2016). For each galaxy in the central region[17] of EL-COSMOS, we convert the provided SEDs from energy units to photon units, then calculate the total number of electrons per second, N_s that will be generated on the detector

$$N_s = A \int f_\lambda T_\lambda e_\lambda \ d\lambda \,, \tag{3}$$

where A is the total collecting area, f_λ is the source flux density as a function of wavelength, T_λ is the atmospheric transmission as a function of wavelength, and e_λ is the product of the total in-band transmission and quantum efficiency as a function of wavelength, in units of $e^-\ \text{photon}^{-1}$. We shall distribute the photons between pixels in Section 2.3.2. As intuition suggested, for the flat instrument configuration, the median source flux is higher in the

redder S band than the bluer L band for all three observing environments (see Figure 5). However, once the wavelength-dependence of SUPERBIT's quantum efficiency is taken into account, the median on-detector flux is higher in L. As will be shown in Section 3, this will further separate the performance of SUPERBIT between red and blue wavelengths.

To predict the detection S/N of each galaxy in a 3×3 pixel aperture[18], we calculate

$$\text{S/N} = \frac{nt\mathcal{F}_p N_s}{\sqrt{nt(\mathcal{F}_p N_s + pN_b + pN_d) + nN_r^2}} \,, \tag{4}$$

where n is the total number of stacked exposures, t is the duration of a single exposure in seconds, $\mathcal{F}_p$ is the fraction of the source intensity that lands inside $p = 3 \times 3 = 9$ pixels on the focal plane, N_s is the total number of electrons per second

---

[17] The EL-COSMOS catalog is divided into 9 area coverage zones for ease of data management. We use the central zone (zone 5), which is already ~1.9 times larger than the field of view of SUPERBIT. Parts of the analysis were repeated on the other zones with no qualitative change in our results, indicating no zone-selection bias.

[18] To check that a 3×3 pixel aperture is a reasonable choice, note that galaxies' median half-light radii are within $0.190''$ and $0.220''$ for all relevant redshifts, the SUPERBIT PSF ranges from $0.200'' - 0.400''$, and that the SUPERBIT detector pixel scale is $0.141''$.
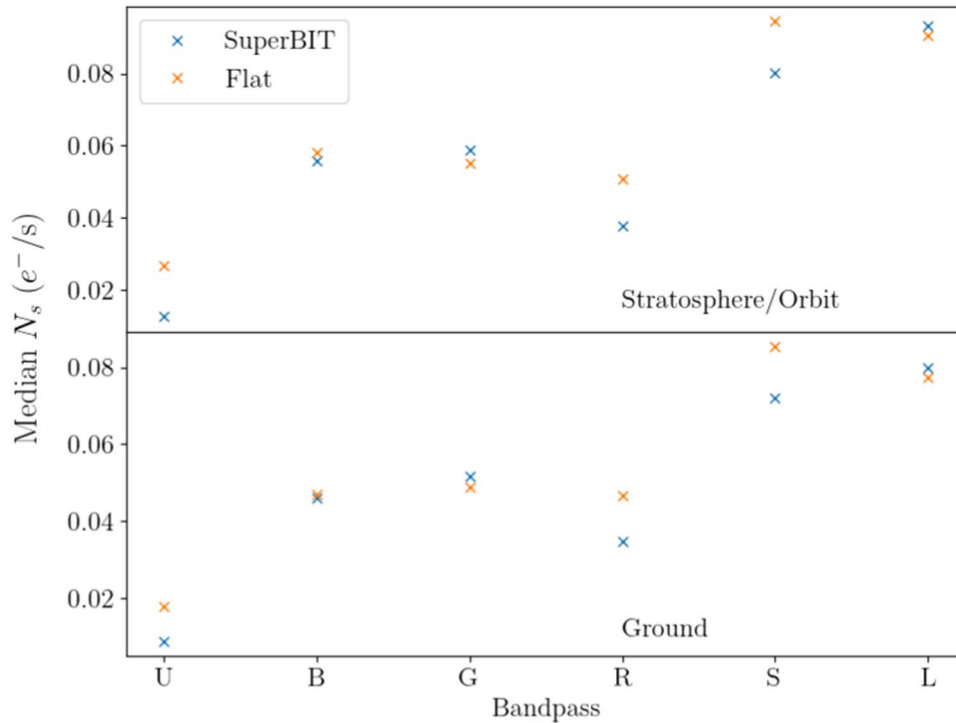
Figure 5. The median number of electrons per second from galaxies in the EL-COSMOS catalog for the SUPERBIT (blue) and flat (orange) configurations for all three observing environments. Note that due to identical atmospheric transmission curves, the values in orbit and stratosphere are identical.

from the observed source, N_b is the number of electrons per second per pixel from the sky background, N_d is the dark current in electrons per pixel, and N_r is the read noise in electrons per pixel. We determined $\{N_s, N_b, N_d, N_r\}$ in previous sections, and the duration of each exposure is dictated by SUPERBIT's pointing and tracking specifications to be $t = 300$ s (see Romualdez et al. 2020). The number of such exposures, n, will be our independent variable. Our figure of merit will be the value of n that guarantees a density of galaxies with $S/N \geqslant 5$ above a threshold (with low n being better).

2.3.2. Assumptions about Galaxy Morphologies and Sizes

To evaluate the figure of merit from Equation (4), we still need to estimate the parameter $\mathcal{F}_p$ for each galaxy. This require knowledge of galaxy morphology that the EL-COSMOS catalog does not provide. We instead exploit fits by Mandelbaum et al. (2012) of each COSMOS galaxy's surface brightness $I(r)$ to a Sérsic (1963) profile

$$I(r) = I_e \exp\left\{-b_n\left[\left(\frac{r}{r_e}\right)^{1/n} - 1\right]\right\}, \qquad (5)$$

where r_e is the radius inside which half of the total light of a galaxy is emitted (also known as the half-light radius), I_e is the source intensity at the half-light radius, n is the Sérsic index parameter, and b_n is a constant determined by the source index. Since our analysis will use all galaxies behind a galaxy cluster at fiducial redshift $z = 0.3$, we determine the median values of r_e and n as a function of redshift (see Figure 6).

We calculate the median value of $\mathcal{F}_p$ as a function of cluster redshift in all SUPERBIT bands, assuming that galaxies have Sérsic profiles with parameters drawn from Figure 6. We convolve these with a PSF, which is modeled as a diffraction-

limited Airy disk centered at the filter's pivot wavelength. In the stratospheric environment, the PSF is also convolved with a Gaussian kernel of width $\sigma = 0.05''$ to represent pointing jitter (Romualdez et al. 2020). We draw both in an 11×11 pixel window, with each pixel over-sampled by a factor of 141×141 (so each subsampled pixel is conveniently 1 ms on a side). We then convolve the galaxy and PSF models and integrate the fraction of flux inside the central 3×3 pixel aperture (see Figure 7). As one would expect for a fixed aperture, the resulting value of $\mathcal{F}_9$ inversely scales with wavelength (see Figure 8), because bluer bands will have a smaller diffraction-limited PSF. This effect also contributes to the red-blue performance discrepancy.[19]

We can now use this information to calculate the number of background sources detected by SUPERBIT when observing a cluster at $z = 0.3$. The result is shown in Figure 9.

2.4. Which Galaxies are Large Enough to be Resolved?

Measurements of weak lensing are only possible for galaxies whose shapes are well resolved. Typically, weak lensing analyses impose size cuts of the form $(R_{gal}/R_{PSF}) > r$, where R_{gal} is some measure of galaxy size, R_{PSF} is some measure of the PSF size, and r is a threshold ratio that depends upon

---

[19] It is important to note that this step induces a nontrivial selection bias in our simulations. In an actual observation the value of p would be dynamically allocated on a source by source basis. However, this step is unavoidable as there currently does not exist public catalogs with sufficient depths to simulate SUPERBIT observations that also provide morphological fits. As a result, we make the most conservative choices to ensure that the selection bias is in favor of larger PSFs (the redder bands) and is therefore dampening the boost in performance gained by the blue bands. The aforementioned choices are: (1) taking the median source shape of all galaxies behind the cluster rather than in a redshift bin thus putting more weight on smaller sources; (2) fixing $p = 9$ rather than dynamically allocating p on a source by source basis thus favoring PSFs with a size closer to $0.423''$.
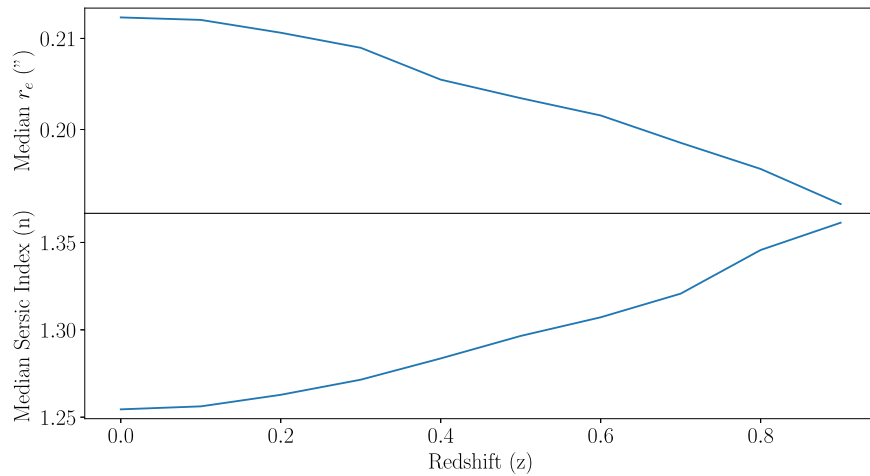
Figure 6. The median Sérsic half-light radius (top panel) and index (bottom panel) of galaxies behind a fixed redshift, as a function of that redshift.
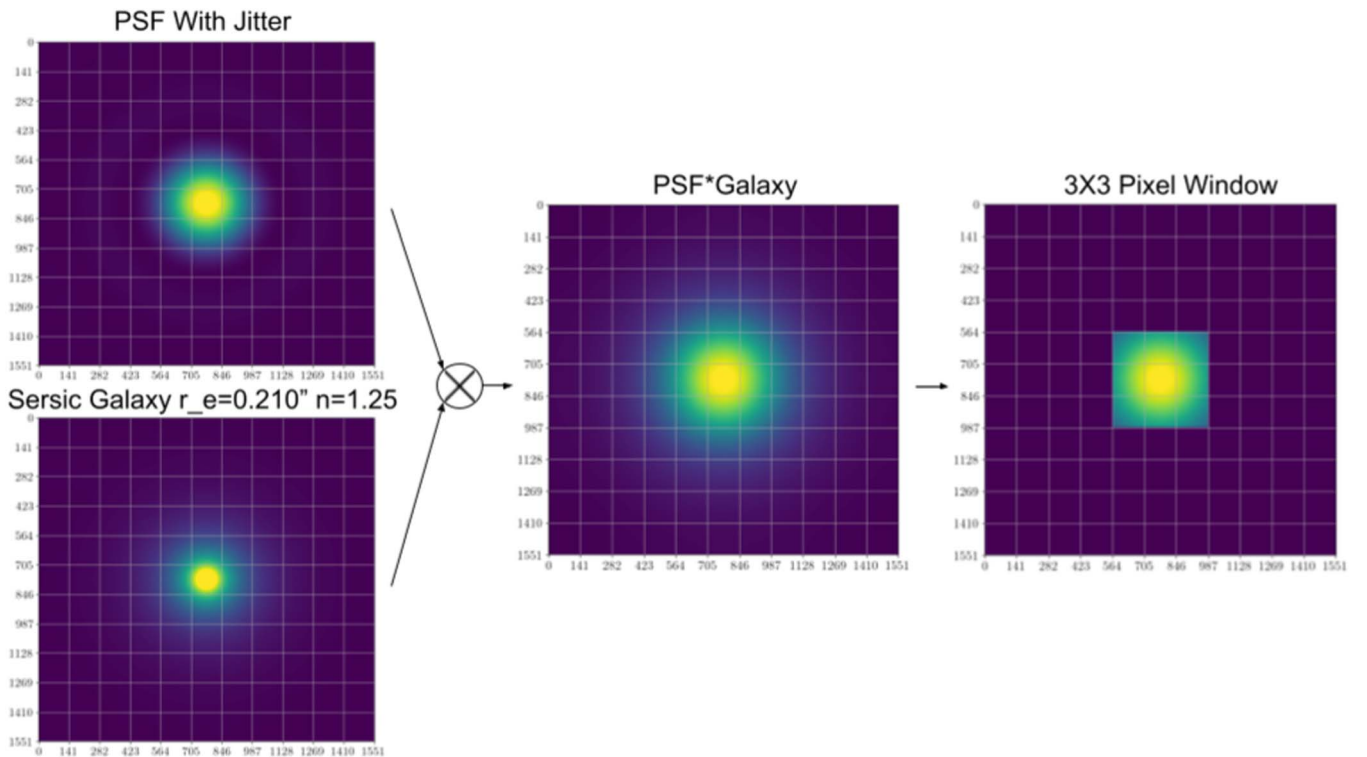

Figure 7. Schematic illustration of the process used to calculate the fraction $\mathcal{F}_9$ of each galaxy's flux that falls within a 3×3 pixel aperture on the focal plane.

mission systematic errors and knowledge of the PSF (Leauthaud et al. 2007; Massey et al. 2013; Zuntz et al. 2018). We perform a version of this size cut using the galaxy half-light radii from Mandelbaum et al. (2012) as R_{gal}, and the PSF FWHM as R_{PSF}. Since this analysis is focused on relative performance of bands, the value of r can be arbitrary, so we set it to be unity. This is equivalent to labeling a source as resolved if its half-light radius is larger than the FWHM of the in-band PSF. Using these assumptions, we calculate the ratio of resolved to detected sources and present the results in Figure 10.

There is an important consideration when evaluating the ratios of resolved to detected galaxies in Figure 10. The Mandelbaum et al. (2012) catalog is shallower than EL-COSMOS, and the relationship between galaxy size and brightness is complex. Therefore, the intrinsic ratio of resolved

to detected galaxies would likely differ between the Mandelbaum et al. (2012) and EL-COSMOS catalogs, had the latter provided galaxy size parameters. This means that the ratio is not directly transferable between catalogs. However, we can reasonably expect that the relative relationship of the ratio of resolved to detected galaxies between bandpasses to change very slowly as a function of catalog depth (this assumption is partially supported by Figure 10).

Therefore, we can transfer the *relative* ratios to EL-COSMOS catalog by folding them into the curves in Figure 9. It is important to note that this transfer renders the absolute scale of the *y*-axis meaningless. Instead of a robust physical prediction of what SUPERBIT could expect to observe in flight, the *y*-axis is abstracted to a metric that only possesses comparative information. However, we did calculate the galaxy densities predicted for HST observations, and check that they roughly
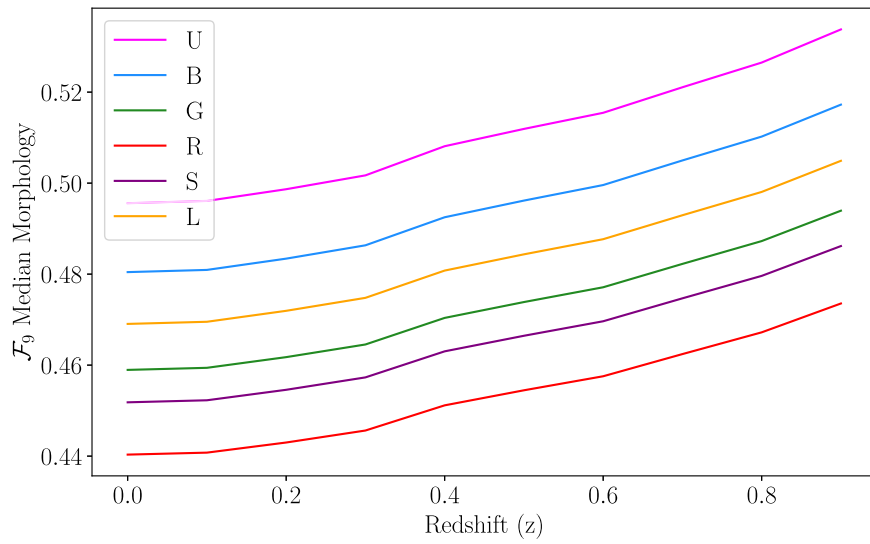
Figure 8. The fraction $\mathcal{F}_9$ of a galaxy's flux that falls within a 3×3 pixel aperture, as a function of cluster redshift for median Sersíc morphology.
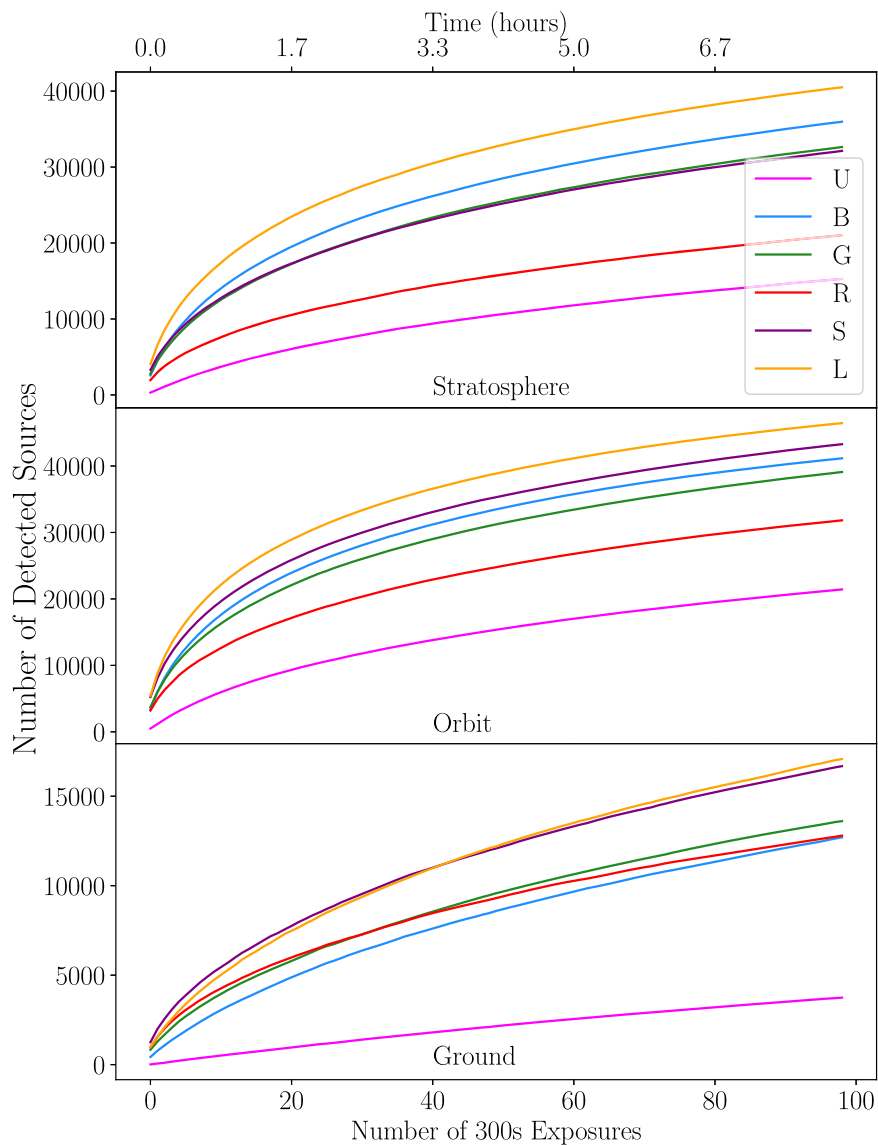

Figure 9. The number of sources with $z > 0.3$ that SUPERBIT can expect to detect if it was to observe the EL-COSMOS zone5 as a function of exposure time. The results are presented in all three relevant environments for each one of the bands presented in Figure 1.
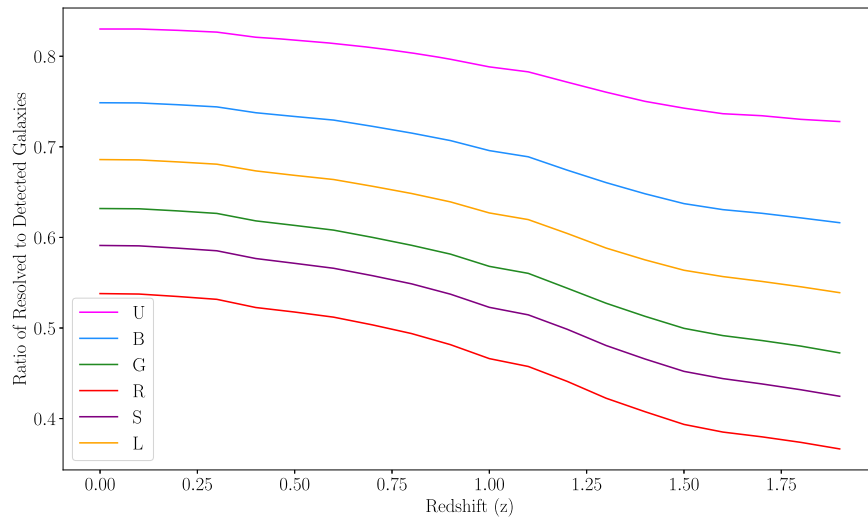
Figure 10. The ratio of resolvable to detectable sources in the Mandelbaum et al. (2012) catalog as a function of redshift for each of SUPERBIT's bands.

match the density (as a function of magnitude) in the Leauthaud et al. (2017) catalog. That suggests the normalization can be meaningful.

To avoid the misinterpretation of the results as a forecast we perform the following normalization. Since SUPERBIT expects to observe each cluster for approximately 3 hr (36 exposures), our normalization will be chosen such that 3 hr of SUPERBIT observations in the stratosphere in the L band will have a metric value of 1.

3. Results

We now have everything we need to evaluate the relative performance of the bands. To do so, we iterate over exposure time by varying the number n of 300 s exposures and calculating the S/N of each EL-COSMOS source at each iteration. We simulate an observation of a cluster at $z = 0.3$ by discarding all sources with redshift $z \leqslant 0.3$, S/N $\leqslant 5$, and $R_{gal} < R_{PSF}$, and count the total number of remaining sources in each band as a function of n. This simulates the number of detected, resolved sources in each band as a function of exposure time (Figure 11).

We recover conventional wisdom that lensing measurements from the ground are most efficient in red bands. For observations from the stratosphere however, we find that bluer L (400–700 nm) and B (370–570 nm) bands are more efficient, because of the diffraction-limited PSF size compared to the ground, and the near-IR sky background compared to low-Earth orbit. As a result of this analysis, the SUPERBIT team has decided to avoid using the redder S band all together and will primarily perform its deep cluster observations in the B band, which has simultaneous utility for estimating photometric redshifts.

3.1. Systematic Errors

We recognize that the redshift uncertainty in the EL-COSMOS catalog increases for dimmer objects. In order to quantify the extent to which this increased uncertainty affects our results, we repeat our analysis on the catalog with various HSC i-band

magnitude cuts. We find that the performance metric ratios between bands is mostly unaffected, as shown in Figure 12.

Additionally, this analysis does not simulate two systematic errors commonly associated with weak lensing observations of galaxy clusters: source blending and background noise due to intracluster light (ICL). We believe that these effects do not appreciably alter our conclusions for the following reasons:

1. Blending effects become more important for observations with larger PSFs. Inclusion of blending would only strengthen the case for observations in the bluer B band, as its smaller PSF enhances the ability to resolve galaxies.
2. Weak lensing measurements are most sensitive to mass distributions projected at 1 Mpc from the cluster center. With SUPERBIT's large field of view, the majority of sources used in WL analysis will lie even farther than this from the cluster's center. At this radius from the cluster center, the ICL is neglible (< 28 mag arcsec^{-2}, see Chu et al. 2022), and should not appreciably decrease the observation depth or increase photometric error.

4. Discussion

This analysis has involved simulating a variety of observing environments, galaxy sizes, detector configurations, and optical bandpasses. These provide sanity checks in familiar observing environments. They are also physically informative, to test how much each effect contributes to our observed red-blue performance discrepancy. To investigate these effects' relative contributions, we toggle the effects creating a variety of effect-free configurations. The configurations considered are the following:

1. *No size cut (r = 0):* in this configuration, we set the size cutoff ratio r to 0 which is equivalent to treating all detected sources as resolved and therefore bluer bands lose the performance advantage gained from having a smaller PSF.
2. *No QE shape (Flat):* in this configuration, the integrated system's quantum efficiency curve is taken to be flat at 0.5 e^- photon^{-1} eliminating the performance advantage
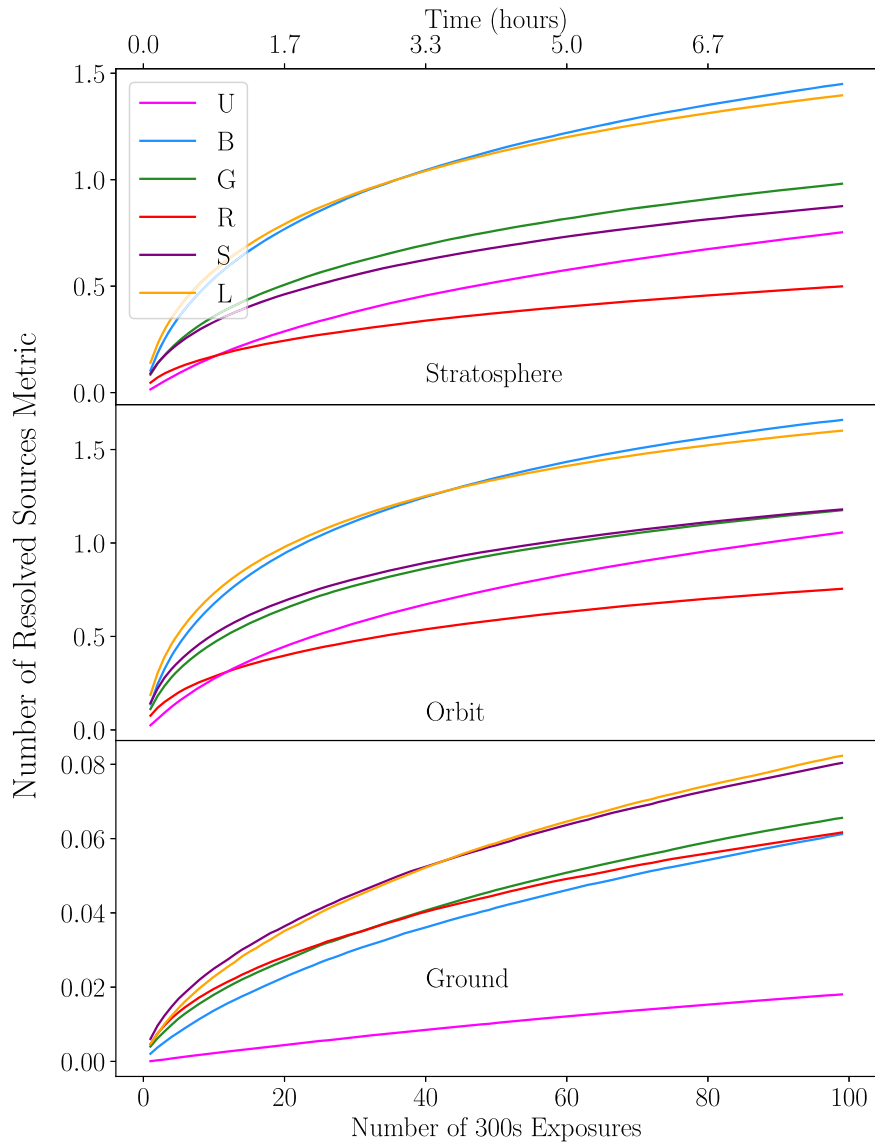
Figure 11. The value of the performance metric for each SUPERBIT band as a function of time, in all three relevant observing environments.
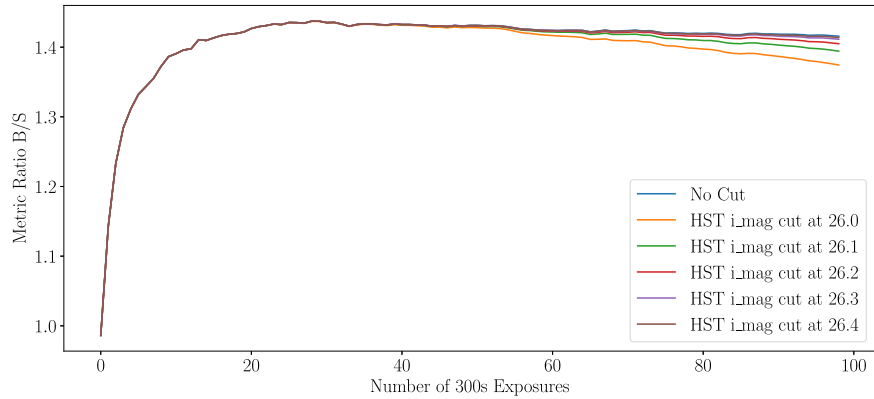

Figure 12. The ratio of the metric value for the *B* and *S* bands in the stratospheric environment as a function number of 300 s exposures with varying brightness cuts applied on the catalog. This figure demonstrates that the bias introduced into our result due to the increasing uncertainty in source redshift is negligible.

blue bands gain due to SUPERBIT s superior sensitivity in the blue.

3. *No background flux ($N_b = 0$)*: in this configuration, the background flux N_b is set to 0 thus eliminating the

performance advantage gained by blue bands due to the bright red background in the stratosphere.

4. *No source smearing ($\mathcal{F}_9 = 1$)*: in this configuration, we enforce that the entire flux from the source lands within
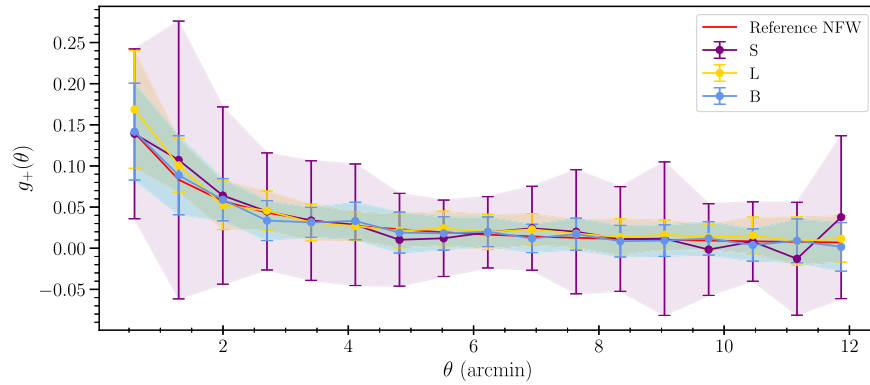
Figure 13. Median tangential shear profiles over 30 simulated observations of a 4.1×10^{14} Msol galaxy cluster at $z = 0.45$. Error bars represent the standard deviation of the mean tangential shear in a radial bin. The red line is the theoretical NFW shear input to all simulations. The variance is more than three times larger in S than B or L.

Table 2
The Performance Metric value after 36 Exposures for Each SUPERBIT Band with Each Effect Independently Toggled off in the Stratosphere

	SUPERBIT	$r = 0$	Flat	$N_b = 0$	$\mathcal{F}_9 = 1$	Raw
U	0.4	0.56	0.61	0.69	0.83	1.73
B	0.98	1.59	0.96	1.69	1.59	3.43
G	0.67	1.41	0.63	1.31	1.16	3.58
R	0.32	0.87	0.34	0.75	0.62	3.2
S	0.6	1.4	0.57	1.34	1.03	3.8
L	1	1.86	0.97	1.8	1.57	3.73

Table 3
This Table is Simply the Result of Dividing Columns 2–6 in Table 2 with the the Corresponding Column 1 entry

	$r = 0/$ SUPERBIT	Flat/ SUPERBIT	$N_b = 0/$ SUPERBIT	$\mathcal{F}_9 = 1/$ SUPERBIT	Raw/ SUPERBIT
U	1.40	1.53	1.73	2.08	4.33
B	1.62	0.98	1.72	1.62	3.50
G	2.10	0.94	1.96	1.73	5.34
R	2.72	1.06	2.34	1.94	10.00
S	2.33	0.95	2.23	1.72	6.33
L	1.86	0.97	1.80	1.57	3.73

Note. This highlights how each each effect contributes to the final result.

the aperture thus eliminating the advantage gained by bluer bands due to lower smearing resulting from smaller PSFs.

5. *Raw flux density:* in this configuration, all the effects mentioned above are turned off (i.e., $r = 0$ with a flat quantum efficiency, no background flux, and no image smearing).

Each of the above effects is toggled on and off, and the metric value at three hours (36 nominal exposures) is calculated in the stratospheric environment. The results of this procedure are presented in Table 2 and Table 3.

This result shows that while all of these effects favor bluer bands, the dominant effects resulting in the superior blue performance are the background, and the PSF size difference at the half meter diffraction limit. Surprisingly, SUPERBIT's superior QE in the blue plays only a minor role.

The SUPERBIT forecasting analysis presented in an upcoming publication, strongly supports the central thesis of this paper. The analysis found that when weak lensing pipeline was run on simulated B images it was able to use 7447 background sources as opposed to the 2578 it was able to use in S images. This result is summarized in Figure 13.

ORCID iDs

Mohamed M. Shaaban https://orcid.org/0000-0002-7600-3190
Ajay S. Gill https://orcid.org/0000-0002-3937-4662
Jacqueline McCleary https://orcid.org/0000-0002-9883-7460
Richard J. Massey https://orcid.org/0000-0002-6085-3780
Eric M. Huff https://orcid.org/0000-0002-9378-3424
Mathilde Jauzac https://orcid.org/0000-0003-1974-8732
David Lagattuta https://orcid.org/0000-0002-7633-2883
Jason S.-Y. Leung https://orcid.org/0000-0001-7116-3710
Johanna M. Nagy https://orcid.org/0000-0002-2036-7008
Susan F. Redmond https://orcid.org/0000-0002-9618-4371
Jason D. Rhodes https://orcid.org/0000-0002-4485-8549
Jürgen Schmoll https://orcid.org/0000-0001-5612-7535
Suresh Sivanandam https://orcid.org/0000-0002-0767-8135

References

Chu, A., Sarron, F., Durret, F., & Márquez, I. 2022, A&A, 666, A54
Dressel, L. 2022, Wide Field Camera 3 Instrument Handbook, Version 14.0 (Baltimore, MD: STScI), https://hst-docs.stsci.edu/wfc3ihb
Gill, A., Benton, S. J., Brown, A. M., et al. 2020, AJ, 160, 266

Gill, A. S., Shaaban, M. M., Tohuvavohu, A., et al. 2022, Proc. SPIE, 12191, 1219114

Haiman, Z., Mohr, J. J., & Holder, G. P. 2001, ApJ, 553, 545

Harvey, D., Massey, R., Kitching, T., Taylor, A., & Tittley, E. 2015, Sci, 347, 1462

Holder, G., Haiman, Z., & Mohr, J. J. 2001, ApJL, 560, L111

Laigle, C., McCracken, H. J., Ilbert, O., et al. 2016, ApJS, 224, 24

Leauthaud, A., Massey, R., Kneib, J.-P., et al. 2007, ApJS, 172, 219

Leauthaud, A., Saito, S., Hilbert, S., et al. 2017, MNRAS, 467, 3024

Mandelbaum, R. 2018, ARA&A, 56, 393

Mandelbaum, R., Hirata, C. M., Leauthaud, A., Massey, R. J., & Rhodes, J. 2012, MNRAS, 420, 1518

Mandelbaum, R., Lackner, C., Leauthaud, A., & Rowe, B. 2012, COSMOS Real Galaxy Dataset, Zenodo, doi:10.5281/zenodo.3242143

Massey, R., Hoekstra, H., Kitching, T., et al. 2013, MNRAS, 429, 661

Massey, R., Kitching, T., & Richard, J. 2010, RPPh, 73, 086901

Robertson, A., Harvey, D., Massey, R., et al. 2019, MNRAS, 488, 3646

Romualdez, L. J., Benton, S. J., Brown, A. M., et al. 2019, arXiv:1911.11210

Romualdez, L. J., Benton, S. J., Brown, A. M., et al. 2020, RScI, 91, 034501

Saito, S., de la Torre, S., Ilbert, O., et al. 2020, MNRAS, 494, 199

Scoville, N., Abraham, R. G., Aussel, H., et al. 2007, ApJS, 172, 38

Sérsic, J. L. 1963, BAAA, 6, 41

Weinberg, D. H., Mortonson, M. J., Eisenstein, D. J., et al. 2013, PhR, 530, 87

Zuntz, J., Sheldon, E., Samuroff, S., et al. 2018, MNRAS, 481, 1149